ACS APPLIED MATERIALS & INTERFACES
Research Article
www.acsami.org

Design and Synthesis of High Performance Multifunctional Ultrathin Hematite Nanoribbons

Debasish Sarkar,* Madhuri Mandal,* and Kalyan Mandal

Department of Condensed Matter Physics and Material Science, S. N. Bose National Centre for Basic Sciences, Block JD, Sector III, Salt Lake, Kolkata 700098, India

Supporting Information

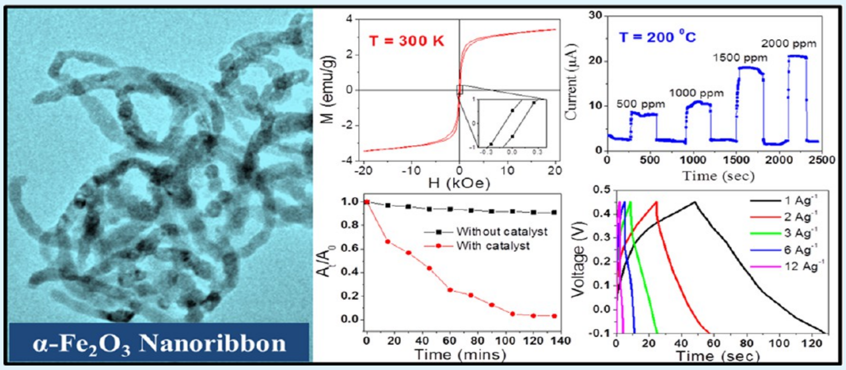

ABSTRACT: 1D porous ultrathin nanoribbons of hematite (α-Fe$_2$O$_3$) were prepared by controlled annealing of different oxides and hydroxides of iron obtained from a solvothermal synthesis method. It is found that calcination at a temperature of 500 °C for 150 min decomposes these iron hydroxides into their most stable oxide form, i.e., α-Fe$_2$O$_3$. Driven by different attractive forces, these porous α-Fe$_2$O$_3$ nanoparticles get aggregated in an ordered fashion to form an ultrathin 1D nanoribbon structure, as observed by detailed time dependent TEM and HRTEM analysis. It has been found that the high aspect ratio and porous surface morphology of these nanoribbons have significantly improved their electronic and spintronic properties as manifested by their photocatalysis, gas sensing, electrochemical, and magnetic behaviors. These hematite nanoribbons exhibit a weak ferromagnetic behavior due to surface spin disorder and shape anisotropy. Lateral confinement of electrons increases the band gap of the nanoribbons, as evident from the UV absorption analysis, which in turn improves their photocatalytic degradation efficiency (rate constant ~0.95 h^{-1}) by delaying the electron−hole recombination process. However, their liquid petroleum gas sensing properties have been found to be mainly governed by the improved (porous) surface of the hematite nanoribbons that provides huge interaction sites for the analyte gas. Most of all, these hematite nanoribbons show a significantly enhanced pseudocapacitive performance exhibited by their high specific capacitance of about 145 F g^{-1} at a current density of 1 A g^{-1}, high rate capability, and also long cycle stability (nearly 96% of capacity retention after 1600 charging/discharging cycles).

KEYWORDS: *ultrathin nanoribbons, solvothermal, phocatalysis, pseudocapacitance*

1. INTRODUCTION

Fabrication of different nanostructures of some semiconducting multifunctional materials has always fascinated researchers because of their versatile range of scientific and technological applications.[1−3] However, the large scale synthesis and also search for some new type of multifunctional materials remains a challenge to the research communities. Among the other transition metal based oxide materials, hematite (α-Fe$_2$O$_3$) has proved itself as the best candidate for multifunctional applications and it has been investigated extensively because of its unique semiconducting properties and different morphology dependent properties that evolve when their size is reduced to a nanometer scale.[4−6] α-Fe$_2$O$_3$ is an n-type semiconductor with an optical band gap (E_g) of 2.14 eV and has been considered to be the most stable iron oxide under ambient condition.[7] Due to its higher thermal stability, low toxicity, and also low production cost, this material has gained extra research attention for its versatile applications in magnetic recording devices,[8] photocatalysis,[4,9,10] gas sensors,[4,11] pigments,[4] water splitting,[12] photodetectors,[13] field emission devices,[14,15] and more importantly in energy harvesting via solar cells[16] and their storage through anode material for supercapacitors and Li-ion batteries.[4,17] Deeply motivated by these intriguing applications, various interesting nanostructures like nanoparticles,[18] nanowires,[3,6,8] nanotubes,[4] nano rods,[16] nano belts,[6] nano rings,[5] nano-hollow spheres,[19] nano bridges,[13] nano flakes,[15] etc. of α-Fe$_2$O$_3$ have been studied and they have been found to exhibit shape and morphology

Received: September 4, 2013
Accepted: November 4, 2013
Published: November 4, 2013

dx.doi.org/10.1021/am403762d | *ACS Appl. Mater. Interfaces* 2013, 5, 11995−12004

dependent unique physical and chemical properties. However, as surface effect becomes dominant in the nano regime, nanostructures that have higher surface to volume ratios and high porosity are more preferable for applications like gas sensing, photocatalytic and electrochemical supercapacitors.[17,20] Actually, this porous surface provides more channels for gas diffusion or mass transport compared to their solid counterpart that enhances their reaction capability and ultimately their performance.[21] In the case of photocatalytic degradation, these pores help for efficient separation of electrons (e^-) and holes (h^+), which otherwise recombine, thus enhancing catalytic efficiency.[20] On the other hand, the porous surfaces of the pseudocapacitor materials and the electrode materials of Li-ion batteries enable diffusion of charge carriers like electrons and cations into and out of it at a higher rate, leading to higher specific capacitance and power density.[17] For these specific reasons, fabrication of 1D porous nanostructures of hematite have gained extra attention because of their large aspect ratio and unique morphology. Moreover, this surface morphology can also be tailored by suitably choosing the synthesis procedures. There are several techniques available for the large scale synthesis of 1D porous hematite nanostructure that are mainly based on template assisted or non-temple chemical routes. However, nontemplate methods like precursor calcination of some hydroxides and carbonates to fabricate porous nanostructures has some extra advantages considering large scale and economical production.[21]

In this present work, we have prepared the 1D porous ultrathin α-Fe_2O_3 nanoribbons by a precursor-calcination technique and investigated their morphology dependent various electronic and magnetic properties. This method of synthesis is much more preferable because it does not need any type of template and can be performed at comparatively lower temperatures. Magnetic properties of these nanoribbons have been found to be strongly affected by the surface spins. Their porous structure and higher surface to volume ratio due to unique 1D structures significantly enhances their photocatalytic, gas sensing, and electrochemical properties, as observed in our research. To the best of our knowledge there has been no such report on the detail study of the multifunctional properties of 1D porous α-Fe_2O_3 nanoribbons till now.

2. EXPERIMENTAL SECTION

2.1. Synthesis of 1D Porous α-Fe_2O_3 Nanoribbons. Here we have synthesized the 1D porous α-Fe_2O_3 nanoribbons by a solvothermal method followed by successive heat treatment of the products. First of all, 2.4 g of $FeCl_3$, $6H_2O$ was mixed in a 60 mL mixture of ethylene glycol and alcohol (2:1) and was stirred magnetically. Then, 1.06 g of urea and 4 mL of oleylamine were added in the solution and the mixture was stirred for 30 min until a complete homogeneous mixture was formed. Then, this mixture was transferred into an 80 mL Teflon lined stainless steel autoclave for the solvothermal procedure. The solvothermal synthesis was carried out for 12 h at a temperature of 180 °C. After the autoclave cooled, the resultant light yellow colored solution was collected and washed in alcohol several times followed by drying in an oven at 65 °C overnight. Finally, this powder sample (precursor) was annealed in a furnace at a temperature of 500 °C for different annealing durations (30, 60, 105, and 150 min). Unlike in other processes for producing α-Fe_2O_3 through calcinations, here we have changed the annealing duration whereas the annealing temperature remains fixed. However, we have chosen only three samples, the precursor, 60 min annealed, and 150 min annealed for further characterization.

2.2. Characterization Techniques. The crystallographic nature of the samples was investigated through X-ray diffraction (Panalytical X'pert pro diffractometer). The morphological and crystalline natures of the samples were studied by transmission electron microscope (TEM, FEI TECNAI TF20ST), high resolution TEM (HRTEM), and selected area electron diffraction (SAED) methods. The elemental composition of the as-prepared nanoribbons was analyzed with X-ray photoelectron spectroscopy (XPS). The magnetic property of the hematite nanoribbons at room temperature was measured in a superconducting quantum interference device (SQUID Quantum design) up to a magnetic field of ± 20 kOe. Optical properties of the samples for band gap calculation and also for photocatalytic efficiency measurement were studied using an ultraviolet−visible spectrometer (SHIMADZU UV-2450). The specific surface area of the hematite nanoribbons and also the pore size distribution was measured by N_2 adsorption−desorption isotherms using Autosorb 1 Quantachrome by the Brunauer−Emmett−Teller (BET) and Barret−Joyner−Halenda (BJH) methods. Prior to the analysis, the powders were degassed at 60 °C and at 1×10^{-4} Torr for 1 h. The gas sensing property of the nanoribbon sample was measured by using a mixture of Ar and oxygen gas in the ratio of 4:1 instead of air and by recording the current by a Keithley source meter (Model: 2400). For this purpose, we made a thin film of the nanoribbon sample on a glass substrate and then the current was measured between two top Au contacts (each having 1 mm of diameter and placed 5 mm apart) at a bias voltage of 5 V. Finally, the electrochemical properties of the hematite nanoribbon sample were investigated with cyclic voltammetry (CV) and galvanostatic (GV) charge/discharge tests by using a software controlled conventional three-electrode electrochemical cell (potentiostat AutoLab-30) consisted of the as-prepared sample as the working electrode, saturated Ag/AgCl as the reference electrode, and a high purity Pt wire as the counter electrode in a 1 M KOH electrolytic solution, at room temperature. To prepare the electrode, the as-prepared nanoribbon sample, acetylene black, and a binder Na−carboxymethyl cellulose (75:15:10) were mixed in de-ionized water to form a slurry. The slurry was then pasted on a copper foil with a blade and was dried in a vacuum oven at 90 °C for 12 h. The CV measurements were performed at different scan rates of 2, 5, 10, 20, 30, 50, and 100 mV s^{-1}, at room temperature. GV charge/discharge measurements were conducted at different current densities of 1, 2, 3, 6, and 12 A g^{-1} within a potential window in the range from −0.1 to +0.45 V to evaluate the specific capacitance, power density, and energy density. The GV charge/discharge method was also employed to test the long-cycle stability of the electrode materials during 1600 cycles at current densities of 1 and 6 A g^{-1}.

3. RESULTS AND DISCUSSION

3.1. Crystallography and Morphology. The crystallinity and phase of the samples at different states of sample preparation was analyzed using X-ray diffraction. The XRD patterns of the samples obtained after the solvothermal method (precursor sample), after 60 min, and after 150 min of heat treatment are shown in Figure 1.

The XRD pattern of the powder sample obtained after the solvothermal method, termed as "precursor" (spectrum i in Figure 1), consists of a mixture of akagenite (β-FeOOH), goethite (α-FeOOH), maghemite (γ-Fe_2O_3), and hematite (α-Fe_2O_3) phases (JCPDS card numbers 34-1266 for β-FeOOH, 29-0713 for α-FeOOH, 39-1346 for γ-Fe_2O_3, and 89-0597 for α-Fe_2O_3 phases).[3,20] However, after 60 min of annealing of the precursor sample, a mixed phase of maghemite and akagenite had been formed (spectrum ii in Figure 1). Interestingly, after 150 min of annealing of the precursor sample in ambient atmosphere, the final sample shows the XRD peaks (spectrum iii in Figure 1) that can be perfectly indexed to a pure rhombohedral phase (space group *R*3*c*) of α-Fe_2O_3 (JCPDS No. 89-0597, $a = 5.039$ Å, $c = 13.77$ Å) without the presence of

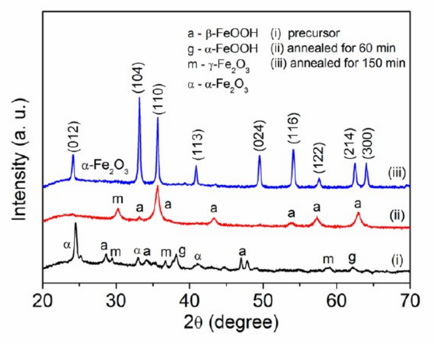

Figure 1. X-ray diffraction patterns of (i) precursor, (ii) sample annealed for 60 min, and (iii) sample annealed for 150 min.

any other impurity phases. The brick red color of the 150 min annealed sample also confirms the formation of hematite. Therefore, this study confirms the formation of hematite (α-Fe_2O_3) after 150 min annealing of the precursor sample.

After the confirmation of crystallinity, the morphological analyses of the samples were carried out using TEM and HRTEM. Here some of representative resultant micrographs are shown in Figure 2 and the morphological changes in other intermediate stages (for 30 min and 105 min annealing durations) are given in the Figure S1 (Supporting information).

The TEM image of the product obtained after the solvothermal process is shown in Figure 2a. From this image, it is evident that the precursor sample consists of a mixture of nanoparticles and nanorods of different dimensions and aspect ratios, respectively. As the as-prepared sample composed of different oxides and hydroxides of iron (evident from the crystallographic analyses), they have different crystallization shape, size, etc., which is why we have a mixture of nanoparticles and nanorods for the precursor sample. However, the 60 min annealed sample mainly composed of nanoparticles have sizes in the range of 20−30 nm. Although the 60 min annealed sample mainly consists of akagenite that has some rodlike crystalline structure, we got nanoparticles, which can be due to the breakage of nanorods into nanoparticles during high temperature annealing procedure. Upon minutely observing, it can be noticed that these nanoparticles have lots of pores that may be generated due to removal of surface adsorbed H_2O or CO_2 during the annealing process.[21] Finally, the TEM image of the 150 nm annealed sample (confirmed as hematite through XRD analysis) shows ribbonlike structures with an average width of ~12 nm as depicted in Figure 2c. These hematite nanoribbons are also porous in nature, which can be seen from Figure 2d. In all other annealing durations, i.e., for 30 and 105 min annealing durations, we have found mixtures of samples having various morphologies, such as mixture of nanorods and nanoparticles were obtained after 30 min annealing and a mixture of nanoparticles and nanoribbons after 105 min of annealing (Supporting information, Figure S1). So, these annealing durations can be considered as the intermediate stages for the formation of nanoribbons. The crystalline phase of the nanoribbons has been confirmed further through high resolution TEM as shown in Figure 2e. The average separation between two consecutive crystal planes has been found to be 0.25 nm that solely corresponds to the [110] crystalline direction of α-Fe_2O_3.[3,18] Figure 2f represents the SAED pattern of the hematite nanoribbons that concludes the single

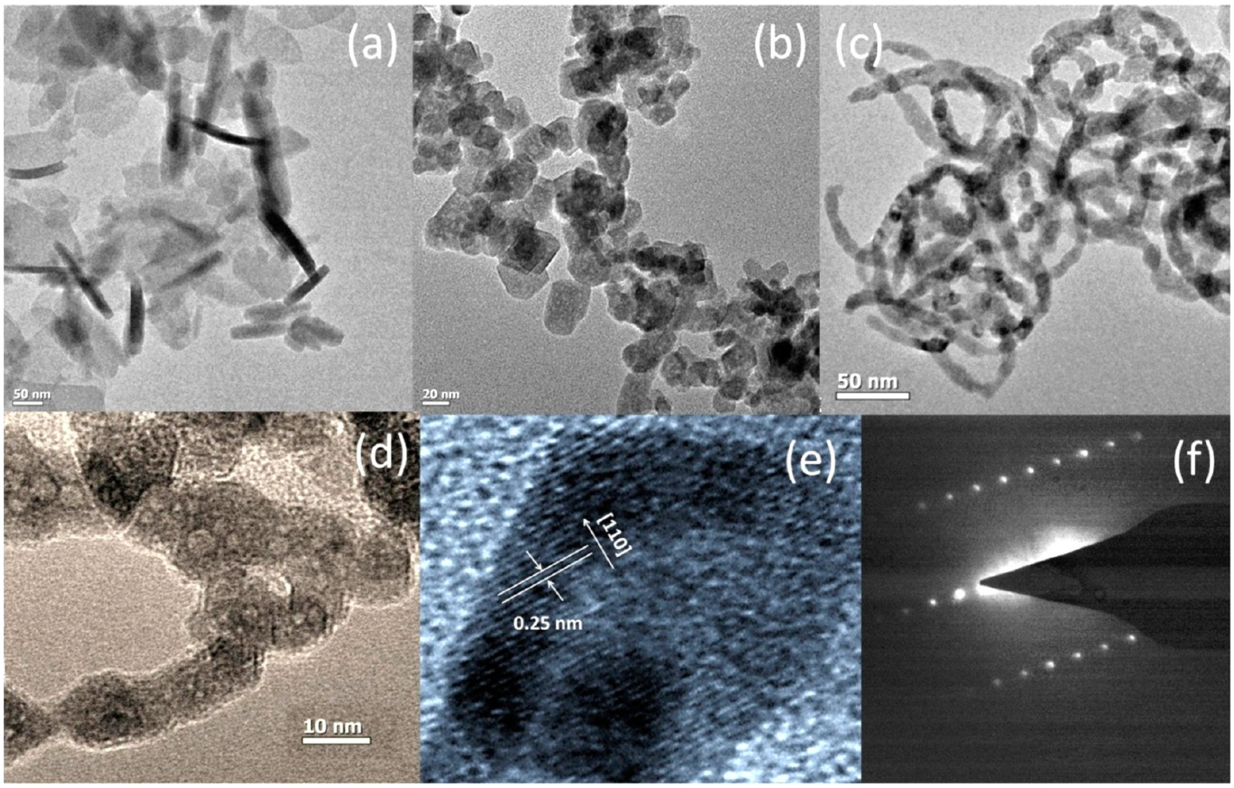

Figure 2. TEM images of (a) precursor, (b) sample annealed for 60 min, (c) sample annealed for 150 min samples, and (d) enlarged version of image c to show the porosity of the materials. (e) High resolution TEM image of the 150 min annealed sample and the corresponding SAED pattern (f).

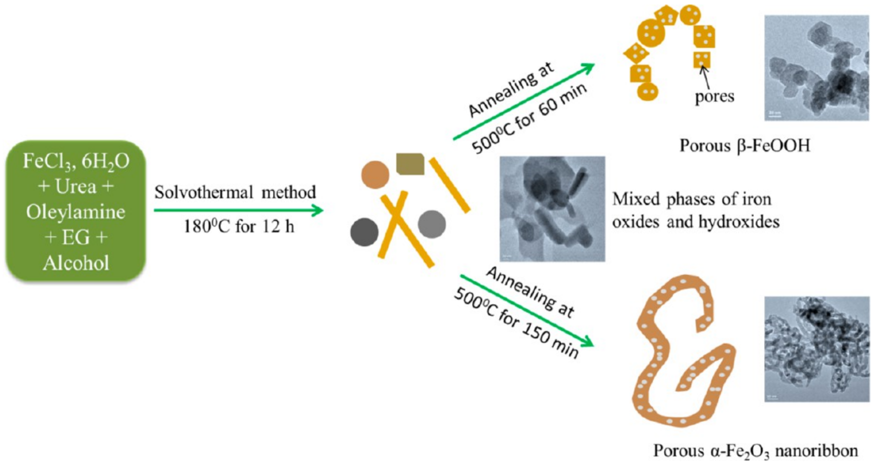

Figure 3. Proposed formation mechanism of 1D porous hematite (α-Fe_2O_3) nanoribbons.

crystalline nature of these nanoribbons. The valence state of iron in α-Fe_2O_3 nanoribbons was further confirmed by X-ray photoelectron spectroscopy (XPS) (Supporting information, Figure S2) in which the Fe $2p_{3/2}$ and Fe $2p_{1/2}$ peaks centered at 711.1 and 724.4 eV, respectively, with another tiny satellite peak at 719.2 eV correspond to the Fe^{3+} oxidation state of Fe.[5,17]

3.2. Formation Mechanism. From the XRD, TEM, and HRTEM analyses, it can be confirmed that the thermal decomposition of different iron oxides and hydroxides at higher temperature leads to the formation of 1D porous α-Fe_2O_3 nanoribbons. However, investigating TEM images at different stages of nanoribbon synthesis, the formation mechanism of the nanoribbons can be summarized as follows: during the solvothermal synthesis phase, ferric chloride in presence of EG, alcohol and urea forms different oxides and hydroxides of iron under higher temperature and pressure, as is evident from the XRD analysis. However, the presence of nanoparticles and nanorods (Figure 2a) is mainly due to different crystallization shapes of these oxides and hydroxides, such as the rodlike structure corresponding to the β-FeOOH crystals. After annealing at 500 °C for 60 min, the unstable phases like maghemite and goethite disappear, and only the akagenite phase predominates. However, such a high temperature breaks the nanorods into smaller crystals, resulting in variable sized nanoparticles at this stage (Figure 2b). Simultaneously, a higher temperature decomposes the absorbed hydroxide and carbonate in the form of H_2O and CO_2, thus creating pores within the nanoparticles. Finally, after further heating at 500 °C for another 90 min (total 150 min), the β-FeOOH decomposes to form nanoparticles of α-Fe_2O_3. Now, the exact mechanism behind the formation of final 1D nanoribbon structure from the primary particles is very difficult to explain. However, various independent factors such as crystal face interaction, electrostatic and dipolar attractions, van der Waals forces, formation of hydrogen bonds, etc. among the primary particles have been proposed to be responsible for this type of self-assembly.[22,23] So, we can assume that these various interactions between these hematite nanocrystals align them in a chainlike form to produce the final nanoribbon structure (Figure 2c). The schematic diagram of the proposed formation mechanism of the hematite nanoribbons is shown in Figure 3.

3.3. Magnetic Properties. The room temperature magnetic hysteresis loop of the α-Fe_2O_3 nanoribbons is shown in Figure 4. The nanoribbons show weak ferromagnetic behavior with very low saturation magnetization ($M_s \sim 3.42$ emu/g) and coercive field ($H_c \sim 96$ Oe), which is in good agreement with other reports where different α-Fe_2O_3 nanostructures have been found to show very weak room temperature ferromagnetism (RTFM).[8,14,24,25] Bulk α-Fe_2O_3 is antiferromagnetic in nature with a Neel temperature and Morin temperature of 950 and 260 K, respectively. However, weak ferromagnetic behavior of the hematite nanoribbons can be ascribed to the surface spin disorder due to broken bonds, self-grown oxygen vacancies, etc. as already observed in many other hematite nanosystems.[8,14] Actually, it has been reported that these oxygen vacancies can induce ferromagnetism by destroying the antiferromagnetic interaction between two neighboring Fe^{3+} sublattices. Similarly in our case, the hematite nanoribbons have lots of crystalline defects, as can be seen from the HRTEM image (Figure 2e) and also have large number of surface spins (due to high surface to volume ratio), which can induce ferromagnetism in the system effectively. Moreover, the unsaturated magnetization curve even at a field of 20 kOe can be due to large shape anisotropy of these nanoribbons.[20]

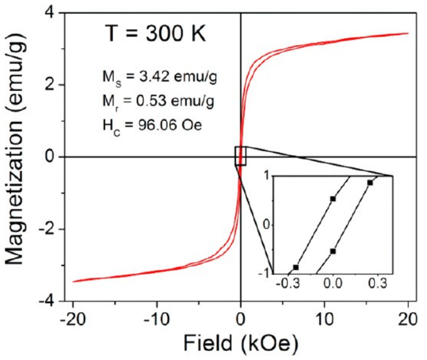

Figure 4. Room temperature hysteresis loop of α-Fe_2O_3 nanoribbons. The inset shows the enlarged portion of the loop near zero fields.

3.4. UV Absorption Analysis: Calculation of Band Gap Energy (E_g). The optical properties of the nanoribbons were studied to observe the effect of size on its band structure, which is very important for understanding their improved functionality over bulk counterpart. To measure the band gap (E_g) of the nanoribbons we have plotted $(\alpha h\nu)^2$ against energy ($h\nu$) as shown in Figure 5. The curve was then fitted with a straight line assuming α^2 is proportional to $(h\nu - E_g)$ for a direct band gap semiconductor like α-Fe_2O_3, where α is the absorption coefficient and $h\nu$ is the energy of photon.[26]

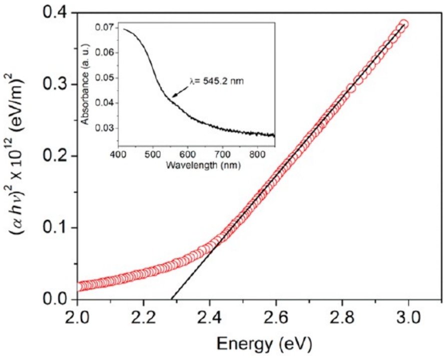

Figure 5. $(\alpha h\nu)^2$ vs energy plot for calculation of band gap of the nanoribbons. The inset shows the corresponding absorption spectra.

From this fitting, the band gap (E_g) of the hematite nanoribbons was found to be ~2.28 eV (λ = 545.2 nm), which is consistent with other reported values for hematite nanoparticles of similar dimensions.[26] This band gap for the nanoribbons was found to be 0.14 eV higher than the bulk value for hematite (E_g = 2.14 eV, λ = 580.8 nm), which can be attributed to the size effect of the hematite nanoribbons, as also seen in case of hematite thin films.[27] When hematite is organized in a quasi-one-dimensional (1D) pattern, the lateral confinement of the charge carriers can result in band broadening near the charge neutrality point.[28] However, this band broadening depends on the width and also the crystallographic orientation of the nanoribbons.[29,30] So, the higher band gap of these nanoribbons increases the electron (e^-)–hole (h^+) recombination process that would be effective for their higher performance towards photocatalytic degradation, as will be discussed shortly.

3.5. Surface Area Measurement. From the TEM images (Figure 2c,d), it is clear that the nanoribbons have highly porous surface structures, which may improve their activity when applied as a catalyst in photocatalytic degradation and also as a gas sensor where surface plays the lead role. Actually, in these cases, a higher surface offers more active sites for the reactions to take place and thus increases the reaction rate. Moreover, the porous surface enhances the possibility of separation of photo-induced electron–hole pairs, which otherwise would have been recombined before the actual reaction.[20] Therefore, before any type of surface related applications of these nanoribbons, it is necessary to determine their exact active surface area and also their porosity. Here we have measured the specific surface area and pore size distribution of these nanoribbons from the N_2 adsorption/desorption isotherms in terms of Brunauer–Emmett–Teller (BET) and Barret–Joyner–Helenda (BJH) methods, as shown in Figure 6.

This isotherm can be classified as a Type IV isotherm, which is the main characteristic for mesoporous materials.[31,32] In this isotherm, the adsorption amount increases gradually for a relative pressure of P/P_0 = 0–0.3 followed by a nearly saturated state for relative pressure up to 0.6. After that, the adsorption amount increases again for a relative pressure of P/P_0 = 0.6–1. The nanoribbons show a high specific surface area of 38 m^2 g^{-1} with a specific pore volume of 0.0163 cc g^{-1}. The average pore size distribution is found to be within 2–3 nm, implying a mesoporous structure of these nanoribbons. Liu et al. have prepared Fe_2O_3 nanofibers with an average surface area of 12 m^2 g^{-1} and shown excellent photocatalytic degradation of Methylene Blue (MB) with these nanofibers.[33] Similarly, the surface area of these hematite nanoribbons is considerably higher than the other reported values for hematite such as hollow spindles (specific surface area of 20.8 m^2 g^{-1}), hollow hematite nanostructures (specific surface area of 16.5 m^2 g^{-1}), etc. In all such cases, these nanostructures have been utilized efficiently for different surface related applications, such as in phenol degradation, for wastewater treatment, etc. Therefore, in this case, we expect that these hematite nanoribbons with high specific surface area can show higher efficiency towards photocatalytic degradation, in gas sensing and also as supercapacitor, i.e., in all surface related phenomena.

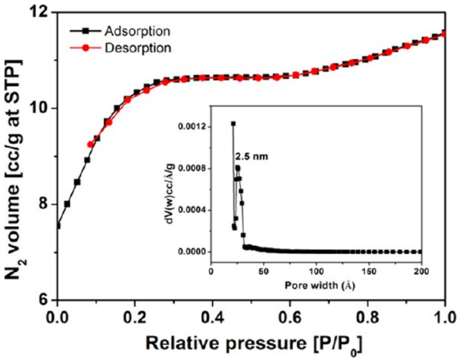

Figure 6. N_2 adsorption/desorption isotherms and corresponding pore size distribution (inset) for the nanoribbons.

3.6. Photocatalytic Activity. The photocatalytic activity of the as synthesized hematite nanoribbons was measured with the Methylene Blue (MB), which is considered the common organic dye in wastewater released from textile industries. In a typical experiment, 2 mg of the sample (hematite nanoribbons) was added in a 50 mL aqueous solution of MB ($[C]_0 = 10^{-5}$ M). Before UV illumination, the mixture was stirred magnetically for 1 h in the dark to establish an adsorption/desorption equilibrium between the catalyst and the MB dye molecules. Then, the solution was placed under a 4 W UV source with λ = 380 nm to initiate the photochemical reaction. After a certain time interval, an about 2–3 mL suspension was collected and centrifuged to separate the catalysts from the MB solution. At last, the concentration of the MB solution was determined by monitoring the maximum absorbance of MB (λ_{max} = 664 nm) using a UV–visible spectrometer. The degradation efficiency (in %) of MB was calculated using the following formula:

$$\text{efficiency (\%)} = \frac{A_0 - A_t}{A_0} \times 100 \tag{1}$$

where A_0 is the MB absorbance at 664 nm at t = 0 and A_t is the absorbance maximum after complete degradation of MB.

The photocatalytic degradation of MB solution at different times by the hematite nanoribbons is shown in Figure 7a. The analysis was performed in two different conditions: (a) without catalyst and (b) with hematite nanoribbons as the catalyst. In absence of the catalyst, the absorbance maximum of MB does not show any significant variation upon UV irradiation. Only 9% of the degradation efficiency was observed upon continuous UV irradiation for 135 min in absence of the catalyst, as shown

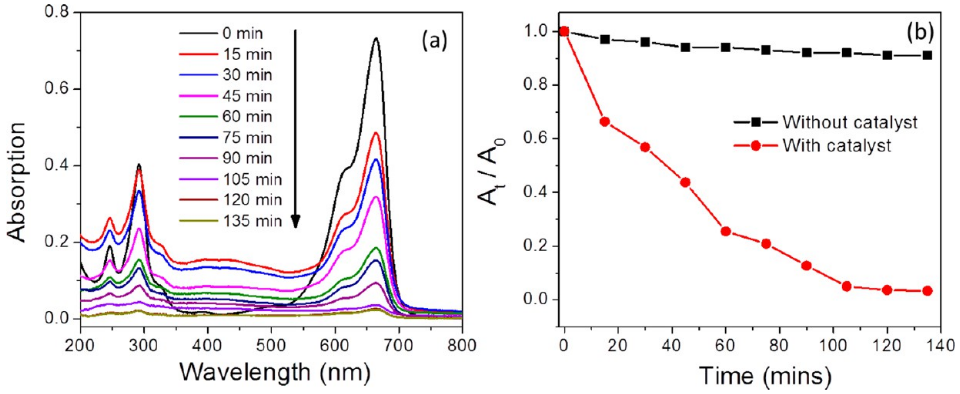

Figure 7. (a) UV−visible absorption spectra of MB during different stages (at 15 min interval) of photocatalytic reaction and (b) photocatalytic degradation of MB as a function of UV irradiation time ($[C]_0$ = 3.2 mg L^{-1}, [catalyst] = 40 mg L^{-1}, at regular pH of 5.6).

in Figure 7b. However, when hematite nanoribbons were used as the catalyst the absorption maximum of MB (at λ = 664 nm) was found to decrease steadily upon UV illumination without any type of peak shift in the absorption maximum (Figure 7a). These results suggest that the degradation and decolorization of the MB dye is mainly due to the presence of nanoribbons (catalyst) upon UV illumination. It has been observed that the decolorization of the solution occurs after nearly 120 min of UV irradiation, and the absorption maximum reduces from 0.73 (at t = 0) to 0.024 during that time. However, there was no change in the absorption intensity upon further UV irradiation for 30 min. The degradation efficiency of the hematite nanoribbons was calculated to be 96.72%. Additionally, the apparent rate constant (k) of the photocatalytic degradation of MB by hematite nanoribbons was calculated by fitting the A_0/A_t vs t plot (shown in Figure 7b) with the first-order rate equation as given below:

$$A_t = A_0 e^{-kt} \tag{2}$$

where A_0 and A_t are the absorption intensities at t = 0 and after complete degradation of MB, respectively. For this study of hematite nanoribbons as catalyst, the apparent rate constant was calculated to be 0.941 h^{-1}. There are several reports on the photocatalytic degradation of MB through α-Fe_2O_3 nanofibers,[33] CdS/α-Fe_2O_3,[34] TiO_2,[35] etc. where they have shown that the structure (surface area) plays a crucial role for enhancing the degradation efficiency. Higher surface and presence of mesopores enhance the possibility of interaction of the dye molecules with the active sites of the catalyst, thus enhancing the degradation efficiency. Similar effects can also be seen in our case as the nanoribbons contain mesopores with a size distribution of 2−3 nm and also have high surface area due to its nanostructure. Moreover, the higher band gap (E_g = 2.28 eV) of these nanoribbons, as evident from the absorption study, can keep the electrons and holes separated for longer times through absorbing UV light, thus reducing the probability of their recombination.[36] During this time, these electrons can effectively migrate to the surface of α-Fe_2O_3 to form hydroxyl radicals ($^\bullet$OH). At first, the oxygen radicals ($^\bullet O_2^-$) might be formed by reaction of electrons with the oxygen adsorbed at the surfaces of α-Fe_2O_3 and then these $^\bullet O_2^-$ might transform to hydroxyl radicals.[37,38] As the $^\bullet$OH is a powerful oxidant, they could easily decompose the methylene blue within a short time.

3.7. Gas Sensing Properties. Being an n-type semiconductor and highly sensitive to gaseous environments, α-Fe_2O_3 has been used widely for detection of combustible and toxic gases present in air. Motivated by the fact that the hematite nanoribbons have a mesoporous structure, we have made an attempt to see the gas sensing properties of these nanoribbons that might be useful for fabrication of sensors. First of all, the optimum operating temperature was measured by sensing 500 ppm LPG within the temperature range 50−300 °C and the results are shown in Figure 8. As the dynamics of sensing reaction strongly influenced by temperature, measurement of the optimum reaction temperature is essential for effective sensing applications. From the figure, one can see that the sensitivity of the hematite nanoribbons sensor increases gradually with increasing temperature and reaches a maximum at a temperature of 200 °C. Therefore, 200 °C is the optimum operating temperature and all the other LPG sensing measurements were performed at this temperature.

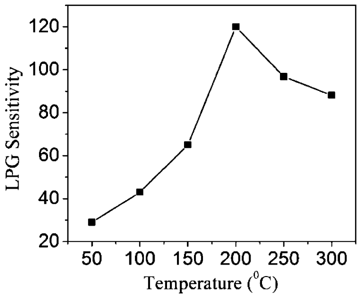

Figure 8. Sensor sensitivities to 500 ppm of LPG under different operating temperatures.

The LPG sensing performance of the nanoribbons with different concentration of gases are also performed, and the dynamic recovery curves are depicted in Figure 9a. The nanoribbons show a response to 500 ppm of LPG, which is exhibited by a sharp change in current value, as shown in Figure 9a. This type of sharp change in current value upon LPG exposure can also be seen at higher LPG concentrations, representing a higher sensing response of the nanoribbons towards LPG. The response, which is the relative change in the current value in LPG exposure, can be calculated through the expression $R = I_{LPG}/I_{air}$, where I_{LPG} and I_{air} are the maximum currents when the LPG flow is "on" and "off",[39] respectively, and the corresponding response curve plotted against different concentrations of LPG is shown in Figure 9b. As evident from the plot, the response of the hematite nanoribbons increases steadily with increasing LPG concentrations.

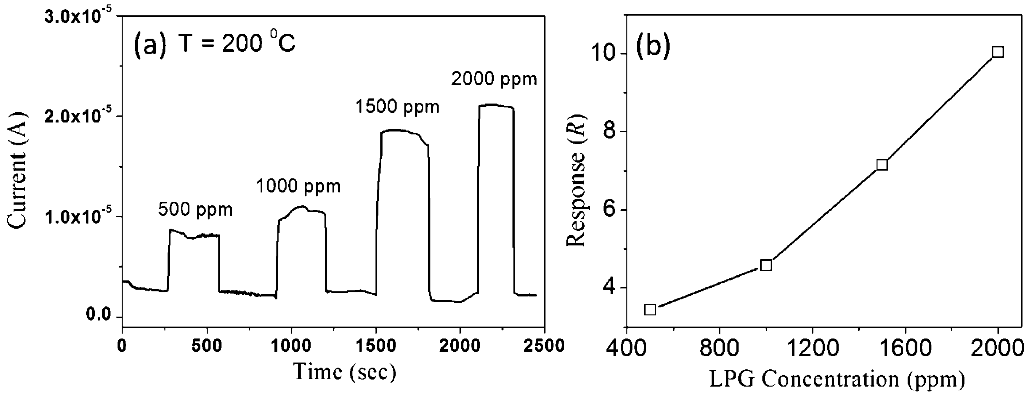

Figure 9. (a) Dynamic response curve of the hematite nanoribbon sensor at different LPG concentrations at T = 200 °C and (b) sensor response to different LPG concentrations at T = 200 °C.

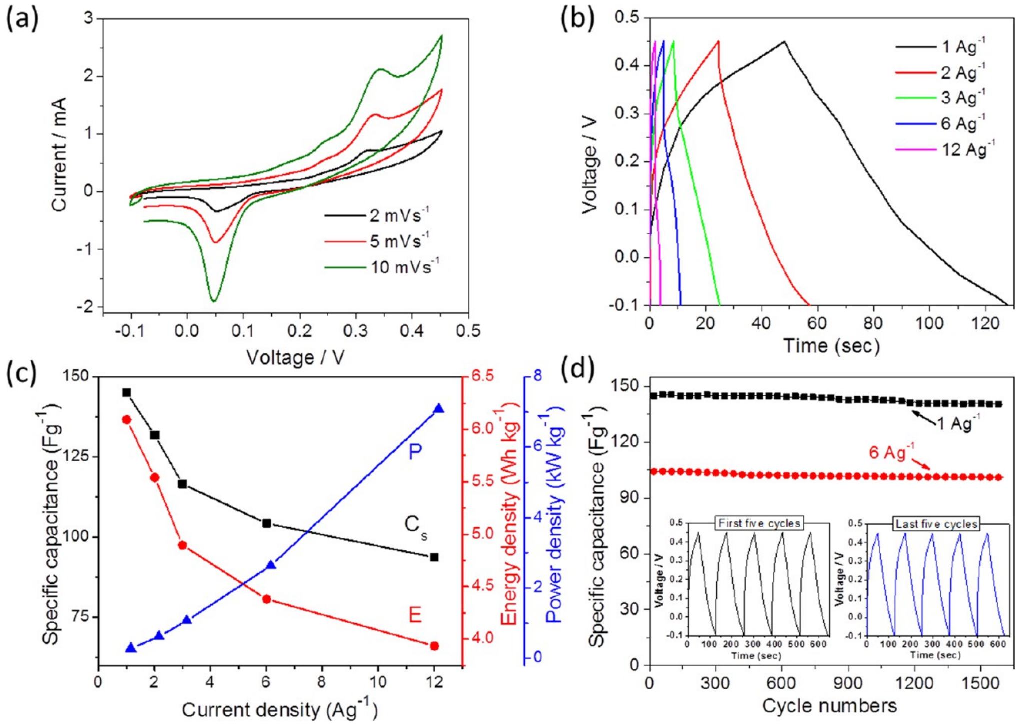

Figure 10. (a) Cyclic voltagrams (CV) of α-Fe_2O_3 nanoribbon electrode at three different scan rates within the voltage limits from −0.1 to +0.45 V, (b) galvanostatic charge/discharge curves for the same electrode at different current densities ranging from 1 to 12 A g^{-1} in 1 M KOH solution within same voltage limits as CV, (c) variation of specific capacitance, energy density, and power density at different current densities, and (d) plot of specific capacitance as a function of cycle number for two different current densities of 1 and 6 A g^{-1}. The inset figures show the charge/discharge profiles of the nanoribbons electrode for the first five cycles and last five cycles at a current density of 1 A g^{-1} within voltage window from −0.1 to +0.45 V.

For oxide semiconductors, the gas sensing property mainly depends on the surface of the nanostructures that actually makes contact with the adsorbed gases, i.e., type of the sensor material, and also the type of the test gas.[40,41] Therefore, better sensing performance can be expected for nanostructures having higher surface areas that are efficient for adsorbing higher amounts of test gases. For n-type semiconductors like ZnO, SnO_2, etc., it has been already established that their sensing mechanism, as manifested by the change in resistance, is mainly governed by the interaction of the analyte gas with the oxygen species mainly O^-, O^{2-}, and O_2^- adsorbed on their surface.[40,42] Similarly, in our case the highly porous surface of the hematite (n-type semiconductor) nanoribbons provide huge active sites for the atmospheric oxygen to combine with the conduction electrons of the semiconductors ($O_2 + e^- \rightarrow O_2^-$, $2O_2^- + e^- \rightarrow 2O^-$, etc.). Actually, these oxygen species localize the mobile electrons from the conduction band (trapping of electrons), thus creating a depletion layer at the surface of the nanoribbons. Now, during the exposure in the LPG, the test gas molecules react with these oxygen species and release the trapped electrons.[39,43] As a result, the electron localization is destroyed and there is an increase in conductivity. However, when the nanoribbons are again exposed to air, relocalization of the conduction electrons by the freshly adsorbed oxygen species leads to decrease in conductivity, as observed in Figure 9a. In addition, the hematite nanoribbon sensor shows a fast recovery within 2 s, representing its superior sensing performance again.

3.8. Pseudocapacitive Performance. The electrochemical properties of the hematite nanoribbons were analyzed in terms of the cyclic voltammetry (CV) and galvanostatic charging/discharging (C/D) methods. All the CV and C/D measurements were carried out in a three electrode cell (described earlier) in 1 M KOH solution. The cyclic voltagrams of the nanoribbon electrode measured within the voltage limits of −0.1 to +0.45 V at different scan rates is shown in Figures 10a and S3 (Supporting information). All the CV loops have a distinct pair of redox (oxidation/reduction) peaks, which is due to the conversion of Fe^{2+} to Fe^{3+} and vice versa, during the anodic and cathodic sweeps of voltage. These types of CV loops are significantly different from those of the nearly rectangular loop characteristics of the electrical double layer capacitors.[44,45] Pseudocapacitance in hematite mainly arises due to the interaction of Fe^{3+} ions with the electrolyte cations, here K^+. Actually, these K^+ ions intercalate into and deintercalate from the surface and almost every channel and pore of hematite nanoribbons and interact with the Fe^{3+} ions, resulting in its pseudocapacitive behavior.[44,45] However, the positions of the redox peaks shift toward more positive and negative voltages with an increase of the scan rate voltage. The area under the CV curves changes significantly with increasing scan rate voltage from 2 to 10 mV s^{-1}, representing higher capacitive performance. It is interesting to note that the shape of the CV curves does not change significantly with increasing the scan rate from 2 mV s^{-1}, indicating low polarization resistance of the nanoribbon electrode because of the higher conductivity of hematite (10^{-4}–10^{-5} S cm^{-1}).[46] Moreover, the nearly liner behavior of the peak current in CV loops with respect to the square root of the scan rate voltage (Supporting Information, Figure S4) represents fast electron transfer during redox reactions; that means the electrochemical process of the electrode is mainly diffusion controlled instead of the kinetic one.[47,48] From CV loops, it can also be seen that the currents of the nanoribbon electrode respond sharply at the switching field, especially at 0.45 V indicating its smaller equivalent series resistance (ESR), which is essential for long rate stability and higher power density of the electrode.[49]

The superior electrochemical performance of this nanoribbon electrode is established further by galvanostatic charge/discharge (C/D) method. As the current density plays an important role in the capacitive performance of this type of pseudocapacitor electrode material, we have done the charge/discharge measurements at different current densities in 1 M KOH electrolyte solution within the voltage range of −0.1 to +0.45 V and are shown in Figure 10b. All the C/D curves are characterized by fast charging and then a relatively slow discharge after reaching the higher voltage limit (here 0.45 V) without any significant voltage drop even at a current density of 6 A g^{-1}, indicating low internal resistance of the electrode. The slow discharge curve with nonlinear slope represents that the faradic reactions are occurred on the surface of this hematite nanoribbon electrode. Additionally, a higher discharging time as compared to charging also represents higher ion/charge transfer capability, i.e., higher Coulombic efficiency (η = discharging time/charging time) of this nanoribbon electrode during faradic reactions.

Now, to have a quantitative idea of the capacitive performance of this hematite nanoribbons electrode, the specific capacitance (C_s) of this electrode material has been calculated at different current densities from the galvanostatic discharge curves using following equation:

$$C_s = \frac{I}{m(\Delta V/\Delta t)} \tag{3}$$

where I is the discharge current (A), Δt is the discharge time (s) consumed in the potential range of ΔV, m is the mass of the active material (or mass of the electrode material) (g), and ΔV is the potential window (V).

The plot of the specific capacitance, calculated from the galvanostatic discharge curves, as a function of current densities for the hematite nanoribbon electrode is shown in Figure 10c. The specific capacitance changes from 145 to 93.65 F g^{-1} as the current density increases from 1 to 12 A g^{-1} with nearly 65% of capacitance retention. Higher specific capacitance at lower current density is mainly because at low current density cations can intercalate on the surface and also can easily penetrate into the innermost portion of the electrode materials through every possible pores and channels more effectively. Specially, the pores of the nanoribbons serve as ion buffering reservoirs that can provide hydroxyl ions (−OH) for sufficient redox reactions even at higher current densities.[17,50] However, decrease of specific capacitance at higher current density is associated with the limited amount of accessible areas for cation diffusion. The outer surface of the electrode material can only be utilized for effective cation intercalation/deintercalation at higher currents. Moreover, high rate capability of this hematite nanoribbon electrode implies that the nanoribbons can withstand fast ion/electron transfer throughout the electrode.[48]

We have also investigated the energy and power response of this nanoribbons electrode that is very essential to fabricate a high performance supercapacitor. The energy density (E (W h kg^{-1})) and the power density (P (kW kg^{-1})) have been calculated using equations given as follows:

$$E = \frac{1}{2} C_s (\Delta V)^2 \tag{4}$$

and

$$P = \frac{E}{t} \tag{5}$$

where C_s (F g^{-1}), ΔV (V), and t (s) are the specific capacitance, potential window of discharge, and time of discharge, respectively. The variation of E and P with current densities for the electrode has also been plotted in Figure 10c. Maximum energy density is found to be ~6.1 W h kg^{-1} at a current density of 1 A g^{-1} whereas it becomes ~4 W h kg^{-1} at a current density of 12 A g^{-1}, implying a good energy storage capacity. The power density of this nanoribbon electrode reaches its highest value of 7 kW kg^{-1} at an energy density of 4 W h kg^{-1}.

Electrochemical stability after a large number of electrochemical cycles, i.e., long cycle life, is another essential characteristic for a high performance supercapacitor. The long cycle stability of this hematite nanoribbon electrode has been evaluated by repeating the charging/discharging measurements at two different current densities of 1 and 6 A g^{-1} within the voltage range of −0.1 to +0.45 V in 1 M KOH solution as depicted in Figure 10d. It is evident from the plots that the specific capacitance remains almost constant after 1600 cycles with only a 4% loss of initial maximum capacitance. The reason behind this decrease of capacitance has been reported to be the mechanical expansion of the electrode material due to continuous insertion/deinsertion of the electrolytic ions into the electrode material or may be due to dissolution of some electrode material after such long cycles. However, in our case the color of the electrolyte didn't change, i.e., no dissolution of hematite, implying a higher electrochemical stability of this hematite nanoribbon electrode.

4. CONCLUSIONS

In a nutshell, we have described a facile technique to fabricate 1D porous ultrathin α-Fe_2O_3 nanoribbons and analyzed their morphology dependent multifunctional properties. The surface of the hematite nanoribbons is found to be highly porous in addition to their high aspect ratio, which increases their effective surface area. All the electronic and magnetic properties of hematite nanoribbons have been significantly affected by their unique morphology. The ferromagnetic nature of these nanoribbons is mainly due to the disorder in surface spins. However, their excellent photocatalytic degradation efficiency and gas sensing properties can mainly be attributed to their improved surface area due to the porous structure. Increase in the optical band gap energy because of their narrow width also has significant effect on their photocatalytic degradation performance. These nanoribbons show excellent psedocapacitive performance manifested by their high specific capacitance, energy density, power density, and long cycle stability, which is mainly because of the higher redox activity of hematite and also due to their unique nanostructure, which allows higher amounts of electrolyte cations to interact at the electrode surface and also into it. So, this type of unique 1D nanostructure of hematite having multifunctional properties accumulated in a single material has huge prospects for versatile fields of applications in the present era of nanoscience and nanotechnology.

■ ASSOCIATED CONTENT

Ⓢ Supporting Information

TEM images of different intermediate stages during the formation of 1D porous α-Fe_2O_3 nanoribbons, XPS characterization of hematite nanoribbons, cyclic voltammetry (CV) curves, and peak current (I) vs square root of scan rate (f) plot for hematite nanoribbon pseudocapacitor measured using CV analysis. This material is available free of charge via the Internet at http://pubs.acs.org.

■ AUTHOR INFORMATION

Corresponding Authors

*D. Sarkar. E-mail: deb.sarkar1985@gmail.com.
*M. Mandal. E-mail: madhuri@bose.res.in.

Notes

The authors declare no competing financial interest.

■ ACKNOWLEDGMENTS

The above work was supported by the Council of Scientific and Industrial Research (CSIR), Government of India, funded project 03(1178)/10/EMR-II. Debasish Sarkar thanks S. N. Bose National Centre for Basic Sciences, Kolkata, India, for providing financial support through Extended Senior Research Fellowship.

■ REFERENCES

(1) Milliron, D. J.; Hughes, S. M.; Cui, Y.; Manna, L.; Li, J. B.; Wang, L. W.; Alivisatos, A. P. *Nature* **2004**, *430*, 190−195.

(2) Agarwal, R. *Small* **2008**, *4*, 1872−1893.

(3) Khan, G. G.; Sarkar, D.; Singh, A. K.; Mandal, K. *RSC Adv.* **2013**, *3*, 1722−1727.

(4) Chen, J.; Xu, L.; Li, W.; Gou, X. *Adv. Mater.* **2005**, *17*, 582−586.

(5) Hu, X.; Yu, J. C.; Gong, J.; Li, Q.; Li, G. *Adv. Mater.* **2007**, *19*, 2324−2329.

(6) Chen, Z.; Cvelbar, U.; Mozetic, M.; He, J.; Sunkara, M. K. *Chem. Mater.* **2008**, *20*, 3224−3228.

(7) Dieckmann, R. *Philos. Mag. A* **1993**, *68*, 725−745.

(8) Kim, C. H.; Chun, H. J.; Kim, D. S.; Kim, S. Y.; Park, J.; Moon, Je Y.; Lee, G.; Yoon, J.; Jo, Y.; Jung, M. H.; Jung, S.; Lee, C. J. *Appl. Phys. Lett.* **2006**, *89*, 223103−223105.

(9) Frank, S. N.; Bard, A. J. *J. Phys. Chem.* **1977**, *81*, 1484−1488.

(10) Ohmori, T.; Takahashi, H.; Mametsuka, H.; Suzuki, E. *Phys. Chem. Chem. Phys.* **2000**, *2*, 3519−3522.

(11) Gou, X. L.; Wang, G. X.; Park, J.; Liu, H.; Yang, J. *Nanotechnology* **2008**, *19*, 125606−125612.

(12) Cesar, I.; Kay, A.; Gonzalez Martinez, J. A.; Grätzel, M. *J. Am. Chem. Soc.* **2006**, *128*, 4582−4583.

(13) Hsu, L. C.; Kuo, Y. P.; Li, Y. Y. *Appl. Phys. Lett.* **2009**, *94*, 133108−133110.

(14) Chueh, Y. L.; Lai, M.W.; Liang, J. Q.; Chou, L. J.; Wang, Z. L. *Adv. Funct. Mater.* **2006**, *16*, 2243−2251.

(15) Zhu, Y.W.; Yu, T.; Sow, C. H.; Liu, Y. J.; Wee, A. T. S.; Xu, X. J.; Lim, C. T.; Thong, J. T. L. *Appl. Phys. Lett.* **2005**, *87*, 023103−023105.

(16) Beermann, N.; Vayssieres, L.; Lindquist, S. E.; Hagfeldt, A. *J. Electrochem. Soc.* **2000**, *147*, 2456−2461.

(17) Sarkar, D.; Khan, G. G.; Singh, A. K.; Mandal, K. *J. Phys. Chem. C* **2013**, *117* (30), 15523−15531.

(18) Lin, M.; Tan, H. R.; Tan, J. P. Y.; Bai, S. *J. Phys. Chem. C* **2013**, *117*, 11242−11250.

(19) Guan, J.; Mou, F.; Sun, Z.; Shi, W. *Chem. Commun.* **2010**, *46*, 6605−6607.

(20) Bharathi, S.; Nataraj, D.; Mangalaraj, D.; Masuda, Y.; Senthil, K.; Yong, K. *J. Phys. D: Appl. Phys.* **2010**, *43*, 015501−015509.

(21) Liu, X.; Zhang, J.; Guo, X.; Wu, S.; Wang, S. *Nanotechnology* **2010**, *21*, 095501−095508.

(22) Politi, Y.; Arad, T.; Klein, E.; Weiner, S.; Addadi, L. *Science* **2004**, *306*, 1161−1164.

(23) Zhong, L. S.; Hu, J. S.; Liang, H. P.; Cao, A. M.; Song, W. G.; Wan, L. J. *Adv. Mater.* **2006**, *18*, 2426−2431.

(24) Jin, J.; Ohkoshi, S.; Hashimoto, K. *Adv. Mater.* **2004**, *16*, 48−51.

(25) Hansen, M. F.; Koch, C. B.; Mørup, S. *Phys. Rev. B* **2000**, *62*, 1124−1135.

(26) Sahana, M. B.; Sudakar, C.; Setzler, G.; Dixit, A.; Thakur, J. S.; Lawes, G.; Naik, R.; Naik, V. M.; Vaishnava, P. P. *Appl. Phys. Lett.* **2008**, *93*, 231909−231911.

(27) Souza, F. L.; Lopes, K. P.; Longo, E.; Leite, E. R. *Phys. Chem. Chem. Phys.* **2009**, *11*, 1215−1219.

(28) Han, M. Y.; Özyilmaz, B.; Zhang, Y.; Kim, P. *Phys. Rev. Lett.* **2007**, *98*, 206805−206808.

(29) Wakabayashi, K.; Fujita, M.; Ajiki, H.; Sigrist, M. *Phys. Rev. B* **1999**, *59*, 8271−8282.

(30) Nakada, K.; Fujita, M.; Dresselhaus, G.; Dresselhaus, M. S. *Phys. Rev. B* **1996**, *54*, 17954−17961.

(31) Fukuoka, A.; Kikkawa, I.; Sasaki, Y.; Shimojima, A.; Okubo, T. *Langmuir* **2009**, *25*, 10992−10997.

(32) Khder, A. E. R. S.; Hassan, H. M. A.; El-Shall, M. S. *Appl. Catal., A* **2012**, *411*, 77−86.

(33) Liu, Y.; Yu, H.; Zhan, S.; Li, Y.; Lv, Z.; Yang, X.; Yu, Y. *J. Sol−Gel Sci. Technol.* **2011**, *58*, 716−723.

(34) Wang, L.; Wei, H.; Fan, Y.; Gu, X.; Zhan, J. *J. Phys. Chem. C* **2009**, *113*, 14119−14125.

(35) Tayade, R. J.; Natarajan, T. S.; Bajaj, H. C. *Ind. Eng. Chem. Res.* **2009**, *48*, 10262−10267.

(36) Grätzel, M. *Nature* **2001**, *414*, 338−344.

(37) Niu, M.; Huang, F.; Cui, L.; Huang, P.; Yu, Y.; Wang, Y. *ACS Nano* **2010**, *4*, 681−688.

(38) Gnaser, H.; Savina, R. M.; Calaway, F. W.; Tripa, E. C.; Veryovkin, V. I.; Pellin, J. M. *Int. J. Mass Spectrom.* **2005**, *245*, 61−67.

(39) Sarkar, S.; Basak, D. *Sens. Actuators, B* **2013**, *176*, 374−378.

(40) Satyanarayana, L.; Reddya, K. M.; Manorama, S. V. *Mater. Chem. Phys.* **2003**, *82*, 21−26.

(41) Xiangfeng, C.; Xingqin, L.; Guangyao, M. *Mater. Sci. Eng., B* **1999**, *64*, 60−63.
(42) Liu, X.; Zhang, J.; Guo, X.; Wu, S.; Wang, S. *Nanoscale* **2010**, *2*, 1178−1184.
(43) Wang, C.; Yin, L.; Zhang, L.; Xiang, D.; Gao, R. *Sensors* **2010**, *10*, 2088−2106.
(44) Simon, P.; Gogotsi, Y. *Nat. Mater.* **2008**, *7*, 845−854.
(45) Zhu, M.; Wang, Y.; Meng, D.; Qin, X.; Diao, G. *J. Phys. Chem. C* **2012**, *116*, 16276−16285.
(46) Hsu, L. C.; Li, Y.-Y.; Hsiao, C.-Y. *Nanoscale Res. Lett.* **2008**, *3*, 330−337.
(47) Yuan, C.; Li, J.; Hou, L.; Zhang, X.; Shen, L.; Lou, X. W. *Adv. Funct. Mater.* **2012**, *22*, 4592−4597.
(48) Wang, D.; Li, Y.; Wang, Q.; Wang, T. *J. Solid State Electrochem.* **2012**, *16*, 2095−2102.
(49) Chen, Z.; Qin, Y. C.; Weng, D.; Xiao, Q. F.; Peng, Y. T.; Wang, X. L.; Li, H. X.; Wei, F.; Lu, Y. F. *Adv. Funct. Mater.* **2009**, *19*, 3420−3426.
(50) Zhang, X.; Shi, W.; Zhu, J.; Zhao, W.; Ma, J.; Mhaisalkar, S.; Maria, T. L.; Yang, Y.; Zhang, H.; Hng, H. H.; Yan, Q. *Nano Res.* **2010**, *3*, 643−652.